Nat. Hazards Earth Syst. Sci. Discuss., 2, 6775–6809, 2014
www.nat-hazards-earth-syst-sci-discuss.net/2/6775/2014/
doi:10.5194/nhessd-2-6775-2014

Natural Hazards and Earth System Sciences
Open Access
Discussions

Modeling rapid mass movements using the shallow water equations

S. Hergarten[1] **and J. Robl**[2]

[1]Universität Freiburg i. Br., Institut für Geo- und Umweltnaturwissenschaften, Freiburg, Germany
[2]Universität Salzburg, Institut für Geographie und Geologie, Salzburg, Austria

Received: 29 September 2014 – Accepted: 13 October 2014 – Published: 4 November 2014

Correspondence to: J. Robl (joerg.robl@sbg.ac.at)

Published by Copernicus Publications on behalf of the European Geosciences Union.

Abstract

We propose a new method to model rapid mass movements on complex topography using the shallow water equations in Cartesian coordinates. These equations are the widely used standard approximation for the flow of water in rivers and shallow lakes, but the main prerequisite for their application – an almost horizontal fluid table – is in general not satisfied for avalanches and debris flows in steep terrain. Therefore, we have developed appropriate correction terms for large topographic gradients. In this study we present the mathematical formulation of these correction terms and their implementation in the open source flow solver GERRIS. This novel approach is evaluated by simulating avalanches on synthetic and finally natural topographies and the widely used Voellmy flow resistance law. The results are tested against analytical solutions and the commercial avalanche model RAMMS. The overall results are in excellent agreement with the reference system RAMMS, and the deviations between the different models are far below the uncertainties in the determination of the relevant fluid parameters and involved avalanche volumes in reality. As this code is freely available and open source, it can be easily extended by additional fluid models or source areas, making this model suitable for simulating several types of rapid mass movements. It therefore provides a valuable tool assisting regional scale natural hazard studies.

1 Introduction

Rapid mass movements such as avalanches, debris flows, and lahars are globally abundant surface processes in steep mountainous areas characterized by high process velocities and large masses of granular material involved (e.g. Kirschbaum et al., 2010). Therefore, rapid mass movements represent first-order threats whenever their process domains intersect with populated areas and infrastructure for transport (streets, railway lines), energy supply (power plants, pipelines, electricity lines) or tourism (e.g. ski resorts). While most of the villages prone to rapid mass movements have already

NHESSD

2, 6775–6809, 2014

implemented hazard mitigation strategies by a combination of permanent and temporal preventive measures, the latter are progressively developed in remote mountainous regions where historical records on rapid mass movements are sparse, so that the level of threat is ambiguous. In combination with field mapping and remote sensing, numerical models describing the motion of granular material on general topography are the primary tool to evaluate the potential impact of rapid mass movements on infrastructure in these remote places. Runout distance, flow and depositional depth, velocity, and momentum of a granular flow resulting from physically based numerical models represent key parameters to (a) delineate hazard zones on regional scale, (b) locate ideal corridors and construction areas for new infrastructure, and (c) develop mitigation strategies for protecting planned and already existing infrastructure against these natural hazards (Hsu et al., 2010; Keiler et al., 2006). To fulfill these tasks codes have to be equipped with advanced numerical techniques to reach the required computational performance (e.g. adaptive mesh refinement), have to provide an interface to geographic information systems (GIS) and should be controllable by a scripting language to perform Monte Carlo simulations and parameter studies for entire valleys and hundreds of process domains.

Several state-of-the-art codes describe granular flow on general topography, but are either not open source (e.g. FLATModel, Medina et al., 2008) or restricted to simple Coulomb-type rheology (e.g. Titan2D, Sheridan et al., 2005). The implementation of a new rheology model even in open-source scientific codes by the user is in general not practicable as a deep knowledge on the specific code and fluid dynamics is required. Other recent codes such as Flow-R (Horton et al., 2013) replace the equations of continuum mechanics by more empirical, grid-based algorithms and thus require a higher degree of calibration.

The Voellmy rheology (Voellmy, 1955) is commonly used to describe debris flows and dense snow avalanches and is implemented in different flavors in commercial software products such as RAMMS (Christen et al., 2010), SAMOS-AT (Sampl and Zwinger, 2004; Sailer et al., 2008; Granig and Jörg, 2012) and ELBA+. The latter has

NHESSD
2, 6775–6809, 2014

been extensively used by the Austrian avalanche and torrent control, but peer-reviewed publications on technical details are still missing. Astonishingly, there are no open-source codes that fulfill all requirements mentioned above to describe granular flow with a Voellmy rheological model on complex topography. In return, there are several open-source packages for a wide range of fluid dynamical problems that provide state-of-the-art flow solvers and a variety of numerical accessories like automatic meshing routines or adaptive mesh refinement, such as OPENFOAM (Weller and Weller, 2008, http://www.openfoam.com), CLAWPACK (LeVeque et al., 2011; Berger et al., 2011, http://clawpack.github.io), and GERRIS (Popinet, 2009, http://gfs.sourceforge.net). Beside many other applications these codes are routinely used to predict the propagation of tsunamis in ocean basins (Popinet, 2012) or to model the extent of inundation areas during flooding (An and Yu, 2012) by solving the nonlinear shallow water equations being the standard approximation for the flow of water in rivers and shallow lakes. These numerical packages are operated by highly flexible parameter files that allow the implementation of new fluid rheology models without writing additional source code, so that it is tempting to describe rapid mass movements with one of these fluid dynamics software packages.

In their spirit, two-dimensional models for rapid mass movements on a given topography are similar to the shallow water equations. In both concepts, vertically averaged velocities are considered, and the rheology of the medium and effects of turbulence are taken into account in form of a friction term depending on flow depth and velocity. However, the widely used shallow water equations are only applicable if the water table is almost horizontal. This condition is in general not satisfied for mass movements in steep terrain, so that more elaborate approaches are required here.

These approaches can be subdivided into two major classes according to the coordinate system used. The different coordinate systems are illustrated in Fig. 1 for the example of a channel not parallel to any of the coordinate axes. The first group of models focuses on flow in a given channel and uses a curvilinear coordinate system where the z axis is always normal to the surface, while the x coordinate follows the so-called

NHESSD
2, 6775–6809, 2014

thalweg in downslope direction (red). A formulation for granular flow in general curved and twisted channels was provided by Pudasaini and Hutter (2003). Recently, an implementation of this concept called r.avalanche in the Open Source GIS GRASS was presented by Mergili et al. (2012). However, it imposes significant simplifications to the thalweg concept, in particular that it is a straight line in map view, so that it is more suitable for flow on slopes than in pre-defined channels. The alternative concept only assumes that the z coordinate is normal to the surface, while the horizontal projections of x and y coordinates approximately follow the original Cartesian axes (blue). The software RAMMS (Christen et al., 2010) implements the simplest version of such a local coordinate system by neglecting the surface curvature. An extension taking the surface curvature into account for the price of more complicated differential equations was presented by Fischer et al. (2012).

In this paper we introduce a different approach based on the original shallow water equations in Cartesian coordinates. Instead of the velocity parallel to the surface, the horizontal component is computed and converted to the velocity parallel to the surface afterwards. The basic problem of this approach, an overestimation of the acceleration, is compensated by introducing an appropriate friction term. In the following section, an expression for this friction term is derived, and in Sect. 4 the approach is validated by comparing several scenarios with the established avalanche model RAMMS.

2 Theory

The shallow water equations provide a two-dimensional approximation for the flow of water (or any liquid or granular medium). They refer to vertically averaged horizontal velocities and assume an almost horizontal water table, so that the vertical component of the velocity can be neglected, and the vertical pressure distribution is hydrostatic. Under these conditions, the horizontal pressure gradient and thus the horizontal acceleration is proportional to the gradient of the water table, resulting in the differential

NHESSD
2, 6775–6809, 2014

equation

$$\frac{\partial}{\partial t}\boldsymbol{v}_\mathrm{h} + (\boldsymbol{v}_\mathrm{h}\cdot\nabla)\boldsymbol{v}_\mathrm{h} = g\boldsymbol{s} - \frac{\tau}{\rho h_\mathrm{v}}\frac{\boldsymbol{v}_\mathrm{h}}{|\boldsymbol{v}_\mathrm{h}|} \tag{1}$$

with

$$\boldsymbol{s} = -\nabla(H + h_\mathrm{v}). \tag{2}$$

The model variables are the vertically averaged horizontal velocity $\boldsymbol{v}_\mathrm{h}$ (a two-component vector) and the vertical (not normal to the surface) flow depth h_v. Both variables depend on the spatial coordinates x and y and on time. The symbol ∇ denotes the two-dimensional gradient operator, and $H(x,y)$ is the topography, so that $\boldsymbol{s}$ is the negative gradient of the water table. The parameters g and ρ are the gravitational acceleration and the density, respectively. The second term at the right-hand side is a friction term in direction opposite to the velocity. Here it is written in terms of a basal shear stress τ, but this does not imply that friction in fact only occurs at the bottom of the fluid layer. For turbulent flow of water, τ is proportional to the square of the velocity, but arbitrary functions involving velocity and flow depth may be used.

If the gradient of the water table is large, the corresponding acceleration term overestimates the real acceleration for two reasons: (i) the real acceleration acts in direction parallel to the surface, while Eq. (1) involves only its horizontal component. (ii) The absolute value of the gradient of the water table, $|\boldsymbol{s}|$, corresponds to the tangent of the slope angle φ,

$$\tan\varphi = |\boldsymbol{s}|, \tag{3}$$

while the downslope acceleration on an inclined plane is in fact proportional to $\sin\varphi$. Compensation of each of these errors requires a multiplication of the acceleration term by a factor $\cos\varphi$.

NHESSD
2, 6775–6809, 2014

The friction term also requires a correction for finite gradients, namely a multiplication by $\cos\psi$ where ψ is the inclination angle of the velocity. This angle is in general smaller than φ and only equal to it for flow in downslope direction. It is given by

$$\tan\psi = \frac{\boldsymbol{v}_\mathrm{h} \cdot \boldsymbol{s}}{|\boldsymbol{v}_\mathrm{h}|}. \tag{4}$$

Furthermore, the vertical flow depth h_v must be replaced by the flow depth normal to the surface that is by a factor $\cos\varphi$ smaller. Returning to the vertical flow depth h_v requires the division of the friction term by $\cos\varphi$.

With these three modifications to the right-hand side, the shallow water equations turn into

$$\frac{\partial}{\partial t}\boldsymbol{v}_\mathrm{h} + (\boldsymbol{v}_\mathrm{h} \cdot \nabla)\boldsymbol{v}_\mathrm{h} = g\cos^2\varphi\boldsymbol{s} - \frac{\tau}{\rho h_\mathrm{v}}\frac{\cos\psi}{\cos\varphi}\frac{\boldsymbol{v}_\mathrm{h}}{|\boldsymbol{v}_\mathrm{h}|}. \tag{5}$$

It should be mentioned that these modifications only extract the vertical components of the acceleration terms at the right-hand side, but do not correct the terms of inertia due to surface curvature.

As our approach shall be compatible with the original shallow water equations, the acceleration term shall remain linear, so that the reduction of the acceleration must be mimicked by an additional friction term

$$\boldsymbol{a} = g\cos^2\varphi\boldsymbol{s} - g\boldsymbol{s} \tag{6}$$

$$= -g\sin^2\varphi\boldsymbol{s}. \tag{7}$$

However, the original shallow water equations only allow a friction term in direction of the velocity. Therefore we only consider the projection of the friction term on the

NHESSD
2, 6775–6809, 2014

velocity,

$$\boldsymbol{a} = -g\sin^2\varphi\boldsymbol{s}\cdot\frac{\boldsymbol{v}_\mathrm{h}}{|\boldsymbol{v}_\mathrm{h}|}\frac{\boldsymbol{v}_\mathrm{h}}{|\boldsymbol{v}_\mathrm{h}|} \tag{8}$$

$$= -g\sin^2\varphi\tan\psi\frac{\boldsymbol{v}_\mathrm{h}}{|\boldsymbol{v}_\mathrm{h}|}, \tag{9}$$

while the component normal to the flow direction is neglected. With this approximation, Eq. (5) turns into

$$\frac{\partial}{\partial t}\boldsymbol{v}_\mathrm{h} + (\boldsymbol{v}_\mathrm{h}\cdot\nabla)\boldsymbol{v}_\mathrm{h} = g\boldsymbol{s} - \left(g\sin^2\varphi\tan\psi + \frac{\tau}{\rho h_\mathrm{v}}\frac{\cos\psi}{\cos\varphi}\right)\frac{\boldsymbol{v}_\mathrm{h}}{|\boldsymbol{v}_\mathrm{h}|}. \tag{10}$$

In the context of dense snow avalanches, the Voellmy rheology (Voellmy, 1955) is the most widely used constitutive law for the friction term. It combines a velocity-independent Coulomb friction term with a term proportional to the square of the velocity as it is mostly used for turbulent flow:

$$\tau = \mu\sigma + \frac{\rho g v^2}{\xi} \tag{11}$$

Here, σ denotes the normal stress at the bottom of the fluid layer. Assuming that the bottom is parallel to the surface, it is given by

$$\sigma = \rho g h_\mathrm{v}\cos^2\varphi. \tag{12}$$

The second term at the right-hand side of Eq. (11) is independent of the direction of the velocity, so that we obtain

$$\tau = \mu\rho g h_\mathrm{v}\cos^2\varphi + \frac{\rho g|\boldsymbol{v}_\mathrm{h}|^2}{\xi\cos^2\psi}. \tag{13}$$

NHESSD
2, 6775–6809, 2014

Inserting this expression in Eq. (10) finally yields

$$\frac{\partial}{\partial t}\boldsymbol{v}_\mathrm{h} + (\boldsymbol{v}_\mathrm{h}\cdot\nabla)\boldsymbol{v}_\mathrm{h} = g\boldsymbol{s} - g\left(\sin^2\varphi\tan\psi + \mu\cos\varphi\cos\psi + \frac{|\boldsymbol{v}_\mathrm{h}|^2}{\xi h_\mathrm{v}\cos\varphi\cos\psi}\right)\frac{\boldsymbol{v}_\mathrm{h}}{|\boldsymbol{v}_\mathrm{h}|}. \quad (14)$$

This set of equations differs from the original shallow water equations (Eq. 1) only by the more complicated friction term (the expression in parentheses at the right-hand side).

3 Implementation

Our approximation can easily be implemented in any continuum fluid dynamics software which is able to solve the shallow water equations for a given bed topography and allows the implementation of arbitrary friction terms. We use the software package GERRIS (http://gfs.sourceforge.net) which is freely available and has been developed for more than ten years. It provides highly developed numerics, and applications of GERRIS have been presented in numerous publications.

Operator splitting provides the simplest way of implementing a nonlinear friction term as the one in Eq. (14). Let us write Eq. (14) in the form

$$\frac{\partial}{\partial t}\boldsymbol{v}_\mathrm{h} + (\boldsymbol{v}_\mathrm{h}\cdot\nabla)\boldsymbol{v}_\mathrm{h} = g\boldsymbol{s} - f(h_\mathrm{v}, \boldsymbol{v}_\mathrm{h}, \varphi, \psi)\boldsymbol{v}_\mathrm{h} \quad (15)$$

with

$$f(h_\mathrm{v}, \boldsymbol{v}_\mathrm{h}, \varphi, \psi) = \frac{g\left(\sin^2\varphi\tan\psi + \mu\cos\varphi\cos\psi + \frac{|\boldsymbol{v}_\mathrm{h}|^2}{\xi h_\mathrm{v}\cos\varphi\cos\psi}\right)}{|\boldsymbol{v}_\mathrm{h}|}. \quad (16)$$

The timestep from t to $t + \delta t$ is now split up into two half steps. In the first half step, an interim solution $\tilde{\boldsymbol{v}}_\mathrm{h}$ (and $\tilde{h}_\mathrm{v}$ as well as the resulting angles $\tilde{\varphi}$ and $\tilde{\psi}$) is computed by

NHESSD
2, 6775–6809, 2014

solving the shallow water equations without friction. In the second half step, the "real" velocity at the time $t + \delta t$ is computed from $\tilde{\boldsymbol{v}}_\mathrm{h}$, $\tilde{h}_\mathrm{v}$, $\tilde{\varphi}$, and $\tilde{\psi}$ by applying the friction term only, i.e. by solving the differential equation

$$\frac{\partial}{\partial t}\boldsymbol{v}_\mathrm{h} = -f(h_\mathrm{v}, \boldsymbol{v}_\mathrm{h}, \varphi, \psi)\boldsymbol{v}_\mathrm{h} \tag{17}$$

where the solution at the time t is the interim velocity $\tilde{\boldsymbol{v}}_\mathrm{h}$. As this equation does not contain any spatial derivatives of the velocity, it is degenerated to a set of ordinary differential equations. Furthermore it does not alter the direction of $\boldsymbol{v}_\mathrm{h}$, so that it is in principle even scalar. Applying a mixed Euler scheme with an explicit discretization of the arguments of f and an implicit discretization to the remaining term $\boldsymbol{v}_\mathrm{h}$, i.e.

$$\frac{\boldsymbol{v}_\mathrm{h}(t+\delta t) - \tilde{\boldsymbol{v}}_\mathrm{h}}{\delta t} = -f(\tilde{h}_\mathrm{v}, \tilde{\boldsymbol{v}}_\mathrm{h}, \tilde{\varphi}, \tilde{\psi})\boldsymbol{v}_\mathrm{h}(t+\delta t) \tag{18}$$

yields the solution

$$\boldsymbol{v}_\mathrm{h} = \frac{\tilde{\boldsymbol{v}}_\mathrm{h}}{1 + \delta t f(\tilde{h}_\mathrm{v}, \tilde{\boldsymbol{v}}_\mathrm{h}, \tilde{\varphi}, \tilde{\psi})}. \tag{19}$$

The angles $\tilde{\varphi}$ and $\tilde{\psi}$ should be computed from the gradient of the surface of the flowing medium (Eq. 2) according to Eqs. (3) and (4) in each timestep. However, the shallow water equations are in principle only valid as long as the gradient of the flow depth is small, i.e. as long as the flow surface is almost parallel to the topography. The corrections introduced in Sect. 2 indeed refer to the inclination of the flow surface, except for the normal stress responsible for the static friction term (Eq. 12) that should rather be related to the topography of the bottom. So in sum, using the gradient of the flow surface should be better than using the gradient of the topography, but practically the difference is minor as all these terms become important only for large gradients where variations in flow depth are less significant than the topographic gradient. As illustrated

NHESSD
2, 6775–6809, 2014

in Sect. 4.1, using the gradient of the flow surface may even generate artefacts if this gradient is not computed from the same discretization scheme that is used internally for solving the shallow water equations, which will likely occur when staggered grids or finite volume discretizations are used. Under this aspect it may be even advisable to use the topographic gradient.

4 Validation

In this section we compare our approximation to the established model RAMMS. We use the simplest version based on Voellmy's rheology, neglecting entrainment (Christen et al., 2010) and do not use the recently introduced features of extending Voellmy's rheology by cohesion and taking into account the effect of surface curvature on the frictional force considered by Fischer et al. (2012). However, all these extensions can in principle be adjusted to our formulation based on the shallow water equations in Cartesian coordinates.

Compared to the reference model RAMMS as defined above, our approach introduces two approximations. The most serious one consists in considering only the horizontal component of the velocity. While the accelerations due to the slope gradient and due to friction are corrected accordingly, the horizontal velocity would remain constant in absence of gravity or friction. As a consequence, the total velocity increases artificially on a convex slope and decreases on a concave slope even without gravitational acceleration. The other simplification concerns applying the correction in acceleration for large slope gradients only in flow direction while leaving the lateral acceleration uncorrected.

In the following we investigate three scenarios defined with regard to these approximations. In the first example, flow down a planar slope is considered. This scenario should be described well by both RAMMS and by our approach. The second set of tests refer to slopes with a strongly curved part in order to examine whether the first

NHESSD
2, 6775–6809, 2014

approximation has a serious effect. Finally we consider a more complex topography as an example being closer to real-world applications.

4.1 Constant flow depth on a planar slope

The movement of an avalanche with a constant flow depth on a planar slope in one dimension can be described by an analytical solution. For this purpose we use the velocity v parallel to the slope and Lagrangian coordinates, which means that v is the velocity of a given particle and not at a given position. Then the equation of motion is the same as for a rigid body,

$$\frac{\partial v}{\partial t} = g\sin\varphi - \frac{\tau}{\rho h}, \tag{20}$$

where τ is the frictional shear stress. According to the arguments leading from Eq. (11) to Eq. (13), this shear stress amounts to

$$\tau = \mu\rho g h\cos\varphi + \frac{\rho g v^2}{\xi}, \tag{21}$$

so that

$$\frac{\partial v}{\partial t} = g\left(\sin\varphi - \mu\cos\varphi - \frac{v^2}{\xi h}\right). \tag{22}$$

The steady-state solution of this equation (i.e. the asymptotic velocity v_∞) is readily obtained by setting the left-hand side to zero:

$$v_\infty = \sqrt{\xi h(\sin\varphi - \mu\cos\varphi)} \tag{23}$$

With this, Eq. (22) turns into

$$\frac{\partial v}{\partial t} = \frac{g}{\xi h}\left(v_\infty^2 - v^2\right). \tag{24}$$

NHESSD
2, 6775–6809, 2014

The time-dependent solution of this equation is

$$v = v_\infty \tanh\left(\frac{t}{T}\right) \tag{25}$$

with the characteristic time

$$T = \frac{\xi h}{g v_\infty} \tag{26}$$

describing how slowly the velocity approaches v_∞.

For testing whether our approach reproduces this behavior correctly, we consider a planar ramp with $\varphi = 30^\circ$ inclination in x direction with Voellmy parameters $\mu = 0.2$ and $\xi = 1000\,\mathrm{m\,s^{-2}}$. The release zone is defined by a rectangular area of 350 m × 400 m (in horizontal projection) at the upper edge of the ramp with a release height of $h = 1$ m measured normal to the topography. Figure 2a shows the topography and the flow depth after 20 s obtained from the simulation with GERRIS where the frictional terms (i.e. the angles φ and ψ in Eq. 14) are computed from the surface of the flowing mass. According to the notation in the GERRIS parameter files, this realization is denoted $\mathrm{GERRIS_H}$ in the following.

Figure 2b compares the longitudinal avalanche profiles of flow depth and flow velocity obtained from three different numerical experiments: the realization $\mathrm{GERRIS_H}$ discussed above, the alternative approach where the bed surface (i.e. the original topography) is used to compute the friction term (denoted $\mathrm{GERRIS_{Zb}}$ in the following), and the reference model RAMMS. Only minor differences between the three models are encountered. The avalanche develops a characteristic tail with a rapidly declining flow depth in up-slope direction, while the initial flow depth of $h = 1$ m is still preserved in the main body. The avalanche has already reached the steady-state velocity of about $18\,\mathrm{m\,s^{-1}}$ in the main body predicted by Eq. (23), while the velocities in the tail are lower as a consequence of the reduced flow depth. The avalanche front of all three experiments is characterized by a slight increase of flow depth and flow velocity

NHESSD
2, 6775–6809, 2014

relative to the main avalanche body. This artefact is in general small, but most pronounced for GERRIS$_H$, while RAMMS and GERRIS$_{Zb}$ show nearly identical profiles at the avalanche front. The slightly stronger artefact occurring in GERRIS$_H$ presumably arises from our simple implementation of the gradient of the fluid surface required for computing the angles φ and ψ required in Eq. (19). Here we use the standard gradient of the fluid surface provided by GERRIS that is computed from simple symmetrical difference quotients. The sophisticated numerics implemented in GERRIS itself used for maintaining a sharp front is not incorporated here, so that finally the driving term of the shallow water equations and the friction term use different schemes of discretization, causing artefacts at the avalanche front where the fluid surface is strongly curved. However, we found in all considered examples that these small artefacts are stable and do not grow through time, so that they are not a serious problem at all.

As a second test, we consider the velocity of the accelerating fluid layer against the time dependent analytical solution (Eq. 25) for different initial flow depths (h), turbulence (ξ) and dry friction (μ) parameters of the Voellmy rheology, and hillslope angles (φ) (Fig. 3). Similarly to the results on the avalanche profiles, the almost perfect agreement between the velocity predicted by Eq. (25) and all sets of numerical experiments verifies the ability of our approach at least for planar slopes. Small deviations occurring shortly after the release scale with the time step size of the numerical model and could be reduced by forcing the flow solver towards smaller time increments. However, these initial small deviations disappear rapidly when approaching the terminal velocity, so that a higher temporal resolution at the expense of increasing computational time does not justify this insignificant benefit in practical applications.

4.2 The effect of profile curvature

While the tests performed in the previous section only concern the technical correctness of the theory and its implementation, the following numerical experiments address the validity and the limitations of the approximations made.

NHESSD
2, 6775–6809, 2014

In order to explore the effects of profile curvature on our approach considering only the horizontal components of the velocity vector (and calculating the total velocity from those) we have performed a series of numerical experiments on curved synthetic topographies and confront the results of our approach with those of RAMMS. The first experiment describes an avalanche on a concave flow path defined by a 30° dipping ramp and a 5° inclined runout zone with a smooth transition between both (Fig. 4). Here and in the following the curvature of the smooth transition zone is defined in such a way that an avalanche entering from the upper ramp with the terminal velocity according to Eq. (23) is exposed to an centrifugal acceleration of about 1 m s^{-2} (which is neglected in both RAMMS and our approach, but considered in detail by Fischer et al., 2012).

The behavior when traveling along the upper ramp is the same as in the example considered in Fig. 2. At $t = 40$ s, the avalanche is characterized by a long tail, while the bulk mass of the avalanche remains undeformed and has reached the steady-state velocity of about 18 m s^{-1} (Fig. 4c and d). At this time the avalanche front approaches the curved transition zone to the gently dipping runout zone leading to a strong deceleration and thickening. At $t = 60$ s, the frontal part of the fluid layer is more than three times thicker than it initially was. The flow velocity has decreased below 10 m s^{-1} everywhere (Fig. 4e and f). At $t = 80$ s, the avalanche thickens further in the runout zone and grows laterally normal to the flow path and in upslope direction as additional mass from the slower avalanche tail becomes incorporated in the deposit. At this stage, significant flow velocities are confined to the steep flow path section where the avalanche tail is still in motion (Fig. 4g and h).

While Fig. 4 shows that the avalanche behaves as expected qualitatively, Fig. 5 provides a quantitative comparison with the reference model RAMMS. The flow depths (Fig. 5a–c) and the velocities (Fig. 5d–f) predicted by both models agree almost perfectly in the domain interesting for hazard assessment, i.e. where the avalanche moves at a significant velocity. The same applies to the runout distance when the avalanche front finally comes to rest.

NHESSD
2, 6775–6809, 2014

Noticeable differences between the results of the GERRIS-based models and RAMMS only occur in the final phase of the avalanche when the front has almost come to rest. While the main body of the avalanche is characterized by a single maximum in the thickness in the GERRIS-based simulations, RAMMS predicts a bimodal avalanche profile. This difference is also reflected in the shape of the final deposits at least when the RAMMS simulation is stopped automatically using the default settings (i.e. when the momentum has decreased to 5 % of its maximum value). However, the difference arises in a phase where only the long tail of the avalanche moves at a considerable velocity, so that material is pushed from behind on the main avalanche body that is almost resting. So this difference is probably not related to the different way of treating velocities, but rather to the different numerical schemes used in RAMMS and GERRIS, and apart from this unimportant for practical purposes.

In Fig. 6, the opposite situation involving a convex topography is considered. Again the release zone is located on a 30° steep slope, but in contrast to the previous experiment the slope steepens in a smooth transition to 45°. The transition from $\varphi_1 = 30^\circ$ to $\varphi_2 = 45^\circ$ causes the fluid layer to accelerate rapidly from $18\,\mathrm{m\,s^{-1}}$ to the new terminal velocity of $21.7\,\mathrm{m\,s^{-1}}$ at a reduced flow depth of 0.83 m. As an effect of our approximation considering only the horizontal components of the velocity vector, the new terminal velocity is reached slightly earlier by GERRIS than by RAMMS. This effect becomes more pronounced by sharp terrain transitions (Fig. 7). In this example, the sharp transition from $\varphi_1 = 30^\circ$ to $\varphi_2 = 45^\circ$ increases the velocity instantaneously to $18\,\mathrm{m\,s^{-1}} \times \frac{\cos 30^\circ}{\cos 45^\circ} = 22\,\mathrm{m\,s^{-1}}$, which is even slightly above the new terminal velocity. However, the avalanche of RAMMS reaches the terminal velocity also rapidly after entering the 45° slope for both the smooth and the sharp transition.

A quantitative estimate on the range where our approximation affects the flow velocity after the slope has changed can be derived from the theoretical considerations made in Sect. 4.1. Instead the velocity as a function of time, we now consider the velocity as

NHESSD
2, 6775–6809, 2014

a function of the traveled distance. Using Eq. (24) we obtain

$$\frac{\partial v}{\partial x} = \frac{\frac{\partial v}{\partial t}}{\frac{\partial x}{\partial t}} = \frac{\frac{g}{\xi h}\left(v_\infty^2 - v^2\right)}{v} \tag{27}$$

$$\approx \frac{2g}{\xi h}(v_\infty - v) \qquad \text{for } v \approx v_\infty. \tag{28}$$

Equation (28) implies that v approaches the terminal velocity v_∞ exponentially with a decay length

$$L = \frac{\xi h}{2g}. \tag{29}$$

In the example considered above, L amounts to about 42 m, so that the avalanche indeed needs a very short traveling distance to approach the terminal velocity. Considering the more realistic situation of a steady-state avalanche with a constant influx instead of a constant flow depth, i.e. $hv = \text{const}$, leads to basically the same result where only the factor 2 in the denominator turns into a factor 3. Thus, the avalanche should practically approach the terminal velocity even more rapidly than stated above.

Returning to Fig. 6, the only significant differences between the results of the two GERRIS-based models and RAMMS occur at a late stage ($t > 80$ s) where the direct effect of our approximation should have almost vanished. As the avalanche becomes more and more stretched at the backward side, the region with a constant thickness becomes shorter until it finally vanishes. In the simulation with $\text{GERRIS}_{\text{Zb}}$, this leads to a rapid decrease in flow depth and consequently in velocity, so that the avalanche decays rapidly. In contrast, RAMMS keeps a sharper distinction between the region of constant flow depth and the tail and consequently maintains the original flow depth and velocity for a longer time. In return, rather strong waves occur at the transition to the tail being visible in both flow depth and flow velocity. Such waves are in principle generated

NHESSD
2, 6775–6809, 2014

by GERRIS$_{Zb}$, too, but with a significantly smaller amplitude than in RAMMS. In return, GERRIS$_{H}$ generates even stronger oscillations than RAMMS.

Similarly to the differences between the models found for the concave topography, the differences found here are presumably not related to our approximation of considering only the horizontal velocity and computing the total velocity afterwards, but rather to the different discretization schemes used in RAMMS and GERRIS. GERRIS itself obviously uses a numerical scheme that is well-suited for reducing oscillations at the transition to the avalanche tail, but our simple implementation of the gradient of the fluid surface used in GERRIS$_{H}$ cannot compete with this scheme.

In sum, the numerical experiments with GERRIS and the comparison with the leading avalanche model RAMMS performed in this section demonstrate the ability of our approach to model avalanches even on curved topography. The effects of our approximations cause only minor deviations, and in particular their impact on predictions of runout distance, flow depth and velocity is practically negligible. The better stability of both the avalanche front and the transition to the tail provides arguments in favor of GERRIS$_{Zb}$ compared to GERRIS$_{H}$.

4.3 Flow over complex topography

The thalweg of rapid mass movements on a real topography is in general curved and twisted. We therefore challenge our approach with the complex topography of a typical alpine avalanche flow path and test the results of our approach against RAMMS. In contrast to the previous examples that are basically one-dimensional, the second approximation made in our theory also becomes relevant here: beyond considering only the horizontal component of the velocity in the equations, our approach only applies corrections for large slopes to the longitudinal component of the velocity.

The hypothetic avalanche is located in the Felbertal, a typical glacially shaped alpine valley with large open flanks between ridges and the tree line representing classical snow avalanche release zones. Deeply incised, curved and twisted gullies canalize the avalanche in one or several branches with locally extreme flow depths. These gullies

NHESSD
2, 6775–6809, 2014

route the granular fluid to the nearly flat valley floor representing the runout zone of the avalanche (Fig. 8).

We compare the maximum values (at each point, taken over the entire simulation) of flow depth, momentum, and velocity of the modeled avalanche. Momentum is defined as the product of flow depth and velocity in this context. We set the release height to $h = 1\,\mathrm{m}$ and define spatially constant parameters for the Voellmy flow resistance law ($\mu = 0.2$, $\xi = 2000\,\mathrm{m\,s^{-2}}$). Generally, the deviations between $\mathrm{GERRIS_{Zb}}$, $\mathrm{GERRIS_{H}}$, and RAMMS are small, and the first-order features of the avalanche agree well between the two GERRIS approaches and RAMMS. This includes flow depths, runout distances, flow velocities, and momentum.

However, a closer examination reveals some second-order deviations between the different numerical approaches. RAMMS shows a more pronounced tendency to overflow counter hillsides and to keep the flow direction even uphill. This is clearly documented at the lower third of the avalanche track where the avalanche is split into two branches. Here the orographic right flow path is characterized by a considerable uphill section. In this domain, the results of RAMMS show higher values in the maximum flow depth compared to the two GERRIS approaches (Fig. 8a–c). The modeled avalanches in RAMMS overflow larger areas causing a wider flow path than predicted by the GERRIS experiments. This is recognized most clearly in the S-shaped gully section. A broader flow path and the tendency to flow uphill observed in avalanches modeled with RAMMS relative to those modeled with $\mathrm{GERRIS_{Zb}}$ and $\mathrm{GERRIS_{H}}$ are caused by larger values in the momentum (Fig. 8d–f) arising from slightly higher flow velocities especially in the gully section of the thalweg (Fig. 8g–i).

In contrast to the small deviations found in the previous examples, this effect is a direct consequence of applying only corrections to the longitudinal acceleration. When an avalanche follows a narrow and strongly curved (in map view) gully, the transversal (centripetal) acceleration preventing the fluid from leaving the gully is overestimated by the shallow water equations, similarly to the longitudinal acceleration. But in contrast to the longitudinal acceleration, the overestimation of the transversal acceleration is not

NHESSD
2, 6775–6809, 2014

corrected, so that the tendency of the avalanche to stay within the gully is stronger than in RAMMS.

A further deviation is observed in the runout zone where the shapes of the avalanche deposit of the RAMMS simulations differ considerably from those of the GERRIS simulations, while the runout distances and base areas of the avalanche deposits of the three models agree well. The discrepancy in the shape of the deposits is similar to that found when considering the runout on the simple concave topography in Sect. 4.2, and it is presumably related to the different numerical schemes used in RAMMS and GERRIS rather than to our approximations. Beyond this, the shape of the deposits may slightly differ because the RAMMS simulations terminate by default when the momentum of the fluid drops below 5 % of the maximum momentum, while the GERRIS simulations were defined to terminate at $t = 240$ s.

Finally, the differences between the realizations GERRIS_{H} where the corrections in the friction term are based an the fluid surface and $\text{GERRIS}_{\text{Zb}}$ where the corrections are computed from the original topography are very small in this example. So the stronger (although not serious) artefacts occurring at the avalanche front in GERRIS_{H} (Sect. 4.1) and the higher stability of $\text{GERRIS}_{\text{Zb}}$ at the transition to the tail remain the only noticeable difference between both GERRIS-based approaches. These differences suggest that using the version $\text{GERRIS}_{\text{Zb}}$ may in general be preferable to GERRIS_{H}.

5 Conclusions

The examples considered in Sect. 4 show that granular avalanches can be simulated using the shallow water equations directly in Cartesian coordinates even in steep terrain if an appropriate additional friction term is included. This finding allows the utilization of software that was originally designed for other purposes, namely modeling the flow of water in rivers, lakes, and oceans.

Compared to software packages explicitly developed for modeling avalanches, a wealth of state-of-the-art fluid dynamics software packages potentially being

NHESSD
2, 6775–6809, 2014

adjustable for this purpose is available. Some of them are even freely available. Therefore, research on avalanches can easily profit from the enormous effort that has already been spent in developing numerical codes in fluid dynamics. The implementations presented in this paper are based on the software GERRIS, but this shall only be seen as an example. Apart from begin freely available and providing state-of-the-art numerics, GERRIS allows the implementation of our method with a moderate effort. However, this shall not imply that GERRIS is indeed the best software for this purpose.

The examples investigated for validation have only revealed minor deviations towards the commercial model RAMMS used as a reference, in particular with regard to the properties of avalanches relevant for hazard assessment. For the artificial, basically one-dimensional geometries investigated in Sects. 4.1 and 4.2, the agreement between our implementations based on GERRIS and RAMMS is even excellent. The small differences between the approaches encountered here are probably not related to the approximations introduced in our theory, but arise from different numerical schemes used for solving the equations of motion. So the approach presented in this study can fully compete with commercial software for mass movements flowing on open flanks or if large volumes and high flow depths occur and small gullies do not influence the flow characteristics strongly. For such geometries the deviations between result of our approach from those of RAMMS are far off from having any implications on the mitigation strategy based on predicted properties of the modeled avalanche.

The example based on a complex topography (Sect. 4.3) reveals still rather small, but perhaps not always negligible differences between our approach and RAMMS. RAMMS solutions show larger flow depths in avalanche tracks with prominent uphill sections and expanded overflowed areas in steep, twisted gullies. In contrast to the differences discussed above, these deviations arise from the approximations discussed in Sect. 3 and represent a small intrinsic model limitation that is inevitable when using the shallow water equation in a Cartesian coordinate system with a friction term acting only in direction opposite to the velocity.

NHESSD
2, 6775–6809, 2014

However, when discussing differences between models on such a small level we should keep in mind that all these modeling approaches involve a considerable inherent uncertainty compared to other flow processes such as the flow of water in lakes and oceans. These uncertainties start with the basic assumption of the granular medium as a single layer continuum and the rheology (e.g. Voellmy's friction law). It continues with the determination of the relevant parameters for dry snow avalanches and does not stop at the determination of the release zone in form of spatial position, extent, and involved volumes (fracture depth). Even the resolution and quality of the applied digital elevation model can highly influence the avalanche path (Bühler et al., 2011), and taking into account further processes such as entrainment introduces an additional uncertainty in the parameters. Assessing these uncertainties quantitatively goes beyond the scope of this paper, but in sum, they are obviously larger than the small deviations between the models.

The differences between the two proposed implementations based on GERRIS are also small. The version GERRIS_{Zb} where the correction terms are computed from the original topography is less prone to artefacts at the avalanche front and at the transition to the tail than the version GERRIS_{H} using the fluid surface, without revealing significant drawbacks anywhere. We therefore suggest to compute the friction terms from the topographic slope instead of the fluid surface.

Although our validation focused on snow avalanches, the approach is in principle also applicable to other rapid mass movements such as debris flows. Debris flows are characterized by lower flow velocities and lower flow path gradients compared to snow avalanches, so that effects of our approximations become even less significant. Beside of model set-ups with a pre-defined release volume, a huge number of scenarios involving different release zones characterized by discharge-time series can be easily implemented within the GERRIS parameter file. In principle the initiation of surface runoff can be defined at each mesh element, so that flooding and debris flow simulations based on precipitation time series for storm events are possible without preceding precipitation runoff models. Flow resistance laws and their parameterizations are also

NHESSD
2, 6775–6809, 2014

defined in the parameter file, so that the implementation of other rheological models (e.g. Bingham fluid) is straightforward and requires no specific coding skills.

We propose that our approach based on GERRIS is suitable for regional scale dense snow avalanche studies on complex terrain and probably also for other types of rapid mass movements. However, dimensioning of permanent protection measures requires numerical models that have been calibrated by the backward analysis of numerous monitored real world avalanches as, for example, performed by the SLF at the Vallèe de la Sionne. In principle, the parameters of the Voellmy fluid model calibrated for RAMMS are fully compatible with our approach, and spatially variable parameter values can be easily implemented in the GERRIS parameter file. This also applies to extensions of the flow law such as the cohesion term implemented in the recent version of RAMMS. Thus, a more or less complete compatibility with RAMMS can be achieved. However, as we did not perform backward analysis calculations to calibrate the fluid model for our approach on our own and tested the compatibility only for a few examples, the modeling results should be taken with caution when mitigation strategies and protection measures are developed. For such applications, the compatibility with established and extensively tested software packages should be ascertained for the given conditions, or at least a careful backward analysis of the specific avalanche should be conducted.

Appendix A: Implementation in GERRIS

The following lines of code show the implementation of our approach in the GERRIS parameter file. Note that the velocities computed here are still the horizontal components and must be converted to velocities parallel to the topography if required. An example of a full implementation (the concave slope considered in Sect. 4.2 is provided in the Supplement).

NHESSD
2, 6775–6809, 2014

```
# Gradient of the original topography (GERRIS_Zb)
# For version GERRIS_H replace "Zb" with "H"
DX = dx("Zb")
DY = dy("Zb")
# tan^2 φ according to Eq. (3)
TAN2PHI = DX*DX+DY*DY
# sin^2 φ from basic trigonometric relations
SIN2PHI = TAN2PHI/(1.+TAN2PHI)
# cos φ from basic trigonometric relations
COSPHI = 1./sqrt(1+TAN2PHI)
# tan ψ according to Eq. (4)
TANPSI = -(DX*U+DY*V)/sqrt(U*U+V*V+eps)
# cos ψ from basic trigonometric relations
COSPSI = 1./SQRT(1+TANPSI*TANPSI)
# Factor 1/(1+δtf) occurring in Eq. (19) with f according to Eq. (16).
F = (P > DRY ? Velocity/(Velocity+dt*GRAV*(SIN2PHI*TANPSI+
mu*COSPHI*COSPSI+Velocity*Velocity/(P*Xi*COSPHI*COSPSI))):0.)
# Multiply both components of the velocity by F according to Eq. (19)
U = U*F
V = V*F
# Magnitude of the 3-dimensioal velocity vector
Vtotal = (P > DRY ? Velocity/COSPSI: 0)
# Flow depth normal to the topography
localDepth = P * COSPHI
```

The Supplement related to this article is available online at doi:10.5194/nhessd-2-6775-2014-supplement.

NHESSD
2, 6775–6809, 2014

Acknowledgements. We thank ILF Consulting Engineers for licensing RAMMS in the course of a common project and the federal government of Salzburg for implementing the INSPIRE guidelines and providing ALS digital elevation models with a resolution of 10 m.

References

An, H. and Yu, S.: Well-balanced shallow water flow simulation on quadtree cut cell grids, Adv. Water Resour., 39, 60–70, doi:10.1016/j.advwatres.2012.01.003, 2012. 6778

Berger, M. J., George, D. L., LeVeque, R. J., and Mandli, K. T.: The GeoClaw software for depth-averaged flows with adaptive refinement, Adv. Water Resour., 34, 1195–1206, doi:10.1016/j.advwatres.2011.02.016, 2011. 6778

Bühler, Y., Christen, M., Kowalski, J., and Bartelt, P.: Sensitivity of snow avalanche simulations to digital elevation model quality and resolution, Ann. Glaciol., 52, 72–80, doi:10.3189/172756411797252121, 2011. 6796

Christen, M., Kowalski, J., and Bartelt, P.: RAMMS: Numerical simulation of dense snow avalanches in three-dimensional terrain, Cold Reg. Sci. Technol., 63, 1–14, doi:10.1016/j.coldregions.2010.04.005, 2010. 6777, 6779, 6785

Fischer, J.-T., Kowalski, J., and Pudasaini, S. P.: Topographic curvature effects in applied avalanche modeling, Cold Reg. Sci. Technol., 74–75, 21–30, doi:10.1016/j.coldregions.2012.01.005, 2012. 6779, 6785, 6789

Granig, M. and Jörg, P.: A dynamic aproach to evaluate the dense and powder snow avalanche model SAMOS-AT, in: 12th Congress Interpraevent, 23–26 April 2012, Grenoble, France, Extended Abstracts, edited by: Koboltschnig, G., Hübl, J., and Braun, J., 196–197, 2012. 6777

Horton, P., Jaboyedoff, M., Rudaz, B., and Zimmermann, M.: Flow-R, a model for susceptibility mapping of debris flows and other gravitational hazards at a regional scale, Nat. Hazards Earth Syst. Sci., 13, 869–885, doi:10.5194/nhess-13-869-2013, 2013. 6777

Hsu, S. M., Chiou, L. B., Lin, G. F., Chao, C. H., Wen, H. Y., and Ku, C. Y.: Applications of simulation technique on debris-flow hazard zone delineation: a case study in Hualien County, Taiwan, Nat. Hazards Earth Syst. Sci., 10, 535–545, doi:10.5194/nhess-10-535-2010, 2010. 6777

NHESSD

2, 6775–6809, 2014

Keiler, M., Sailer, R., Jörg, P., Weber, C., Fuchs, S., Zischg, A., and Sauermoser, S.: Avalanche risk assessment – a multi-temporal approach, results from Galtür, Austria, Nat. Hazards Earth Syst. Sci., 6, 637–651, doi:10.5194/nhess-6-637-2006, 2006. 6777

Kirschbaum, D. B., Adler, R., Hong, Y., Hill, S., and Lerner-Lam, A.: A global landslide catalog for hazard applications: method, results, and limitations, Nat. Hazards, 52, 561–575, doi:10.1007/s11069-009-9401-4, 2010. 6776

LeVeque, R. J., George, D. L., and Berger, M. J.: Adaptive mesh refinement techniques for tsunamis and other geophysical flows over topography, Acta Numer., 20, 211–289, doi:10.1017/S0962492911000043, 2011. 6778

Medina, V., Hürlimann, M., and Bateman, A.: Application of FLATModel, a 2D finite volume code, to debris flows in the northeastern part of the Iberian Peninsula, Landslides, 5, 127–142, doi:10.1007/s10346-007-0102-3, 2008. 6777

Mergili, M., Schratz, K., Ostermann, A., and Fellin, W.: Physically-based modelling of granular flows with Open Source GIS, Nat. Hazards Earth Syst. Sci., 12, 187–200, doi:10.5194/nhess-12-187-2012, 2012. 6779

Popinet, S.: An accurate adaptive solver for surface-tension-driven interfacial flows, J. Comput. Phys., 228, 5838–5866, doi:10.1016/j.jcp.2009.04.042, 2009. 6778

Popinet, S.: Adaptive modelling of long-distance wave propagation and fine-scale flooding during the Tohoku tsunami, Nat. Hazards Earth Syst. Sci., 12, 1213–1227, doi:10.5194/nhess-12-1213-2012, 2012. 6778

Pudasaini, S. P. and Hutter, K.: Rapid shear flows of dry granular masses down curved and twisted channels, J. Fluid Mech., 495, 193–208, doi:10.1017/S0022112003006141, 2003. 6779

Sailer, R., Fellin, W., Fromm, R., Jörg, P., Rammer, L., Sampl, P., and Schaffhauser, A.: Snow avalanche mass-balance calculation and simulation-model verification, Ann. Glaciol., 48, 183–192, doi:10.3189/172756408784700707, 2008. 6777

Sampl, P. and Zwinger, T.: Avalanche simulation with SAMOS, Ann. Glaciol., 38, 393–398, doi:10.3189/172756404781814780, 2004. 6777

Sheridan, M. F., Stinton, A. J., Patra, A., Pitman, E. B., Bauer, A., and Nichita, C. C.: Evaluating Titan2D mass-flow model using the 1963 Little Tahoma Peak avalanches, Mount Rainier, Washington, J. Volcanol. Geoth. Res., 139, 89–102, doi:10.1016/j.jvolgeores.2004.06.011, 2005. 6777

NHESSD

2, 6775–6809, 2014

Voellmy, A.: Über die Zerstörungskraft von Lawinen, Schweiz. Bauzeitung, 73, 159–165, 212–217, 246–249, 280–285, 1955. 6777, 6782

Weller, H. and Weller, H. G.: A high-order arbitrarily unstructured finite-volume model of the global atmosphere: tests solving the shallow-water equations, Int. J. Numer. Fl., 56, 1589–1596, doi:10.1002/fld.1595, 2008. 6778

NHESSD

2, 6775–6809, 2014

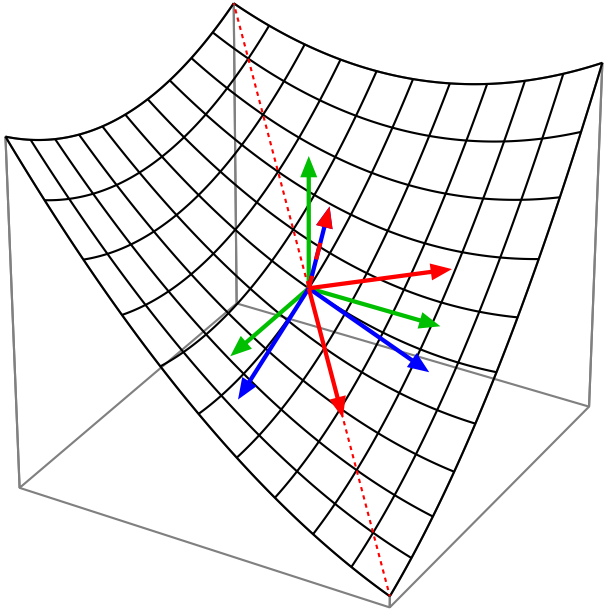

Figure 1. Different coordinate systems used for modeling mass movements in a channel not parallel to any of the Cartesian coordinate axes. Green: Cartesian coordinates (this study). Blue: coordinates aligned to the surface (x and y parallel to the surface, z normal to the surface). Red: coordinates aligned to the surface where the x axis follows the thalweg (dashed red line).

NHESSD
2, 6775–6809, 2014

Modeling rapid mass movements using the shallow water equations

S. Hergarten and J. Robl

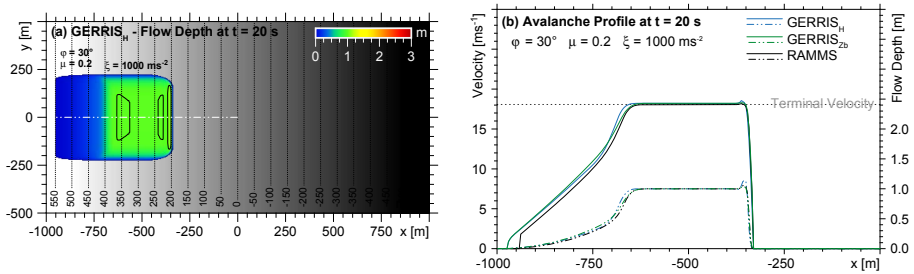

Figure 2. Comparison of two different numerical solutions of GERRIS with RAMMS for granular flow over a 30° dipping ramp for Voellmy parameters $\mu = 0.2$ and $\xi = 1000\,\mathrm{m\,s^{-2}}$ and an initial flow depth $h = 1\,\mathrm{m}$. **(a)** Two-dimensional representation of the ramp geometry and the flow depth of the fluid layer measured normal to the surface after 20 s. The white dashed-dotted line indicates the position of the longitudinal profiles shown in **(b)**. **(b)** Longitudinal profiles of three different numerical models showing flow velocity (solid lines) and flow depth (dashed-dotted lines). The gray dashed line indicates the theoretical terminal velocity according to Eq. (23). GERRIS-based models (blue and green lines) apply gradients of fluid surface ($\mathrm{GERRIS_H}$) and gradients of the topography ($\mathrm{GERRIS_{Zb}}$) respectively, and black lines are results of RAMMS as reference.

NHESSD
2, 6775–6809, 2014

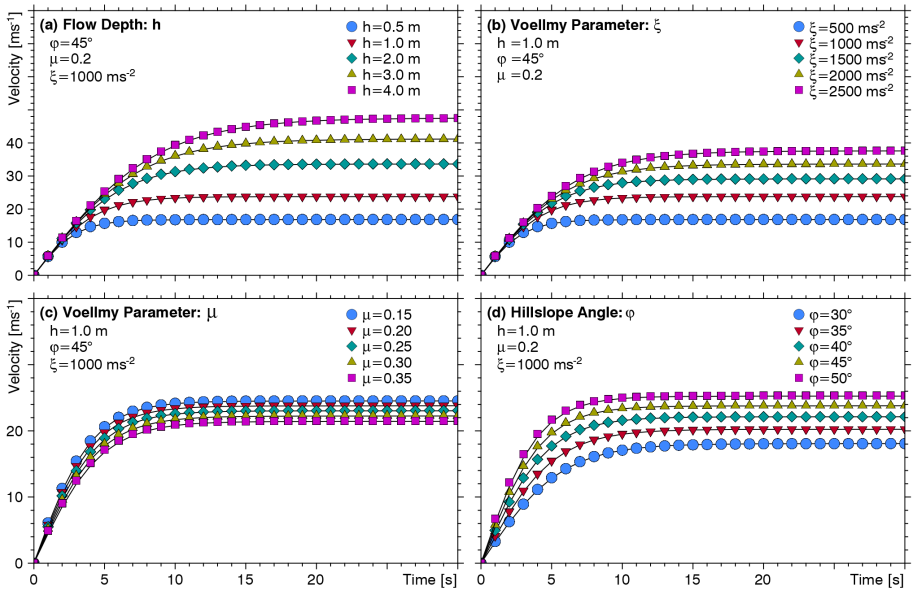

Figure 3. Test of the numerical results of GERRIS$_{Zb}$ (symbols) against the one-dimensional analytical time dependent solution for a Voellmy fluid flowing on a flow path with a constant slope (Eq. 25, solid lines) for several parameter sets for **(a)** flow depth h, **(b)** turbulence parameter ξ, **(c)** dry friction parameter μ, and **(d)** slope angle φ.

NHESSD
2, 6775–6809, 2014

Modeling rapid mass movements using the shallow water equations

S. Hergarten and J. Robl

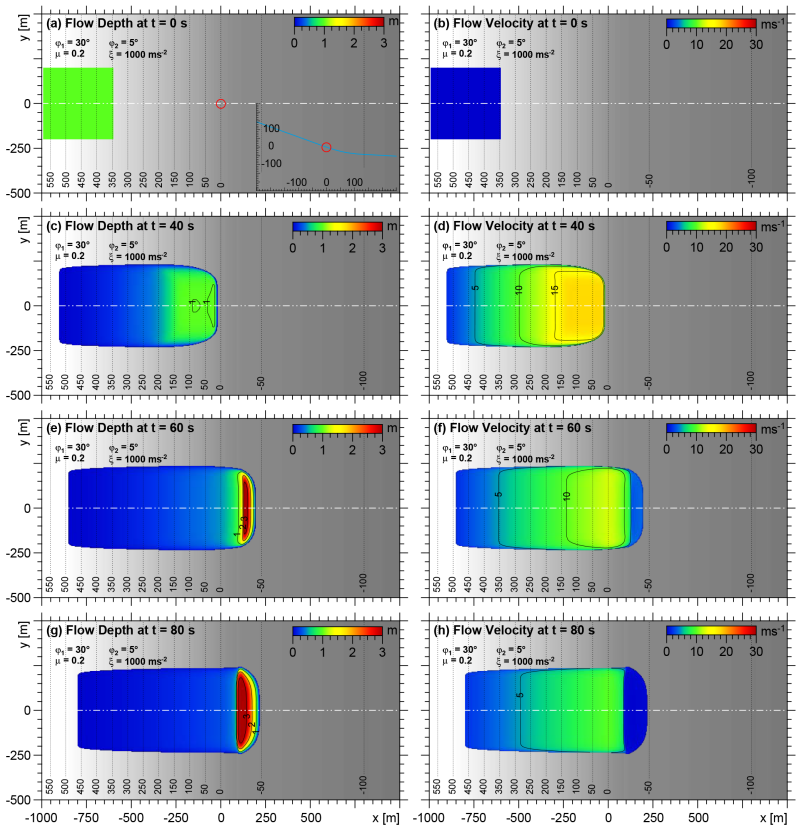

Figure 4. Two-dimensional representation of numerical solutions of GERRIS$_{Zb}$ for flow depth and flow velocity of a partly concave slope at four different time steps. The fluid layer accelerates at an inclined ramp ($\varphi_1 = 30^\circ$) and runs out in a gently dipping surface ($\varphi_2 = 5^\circ$) with a smooth transition. A topographic profile of the geometry is shown in the inset of **(a)**. The white dashed-dotted line indicates the position of the longitudinal profiles shown in Figs. 5 and 6.

.

NHESSD
2, 6775–6809, 2014

Modeling rapid mass movements using the shallow water equations

S. Hergarten and J. Robl

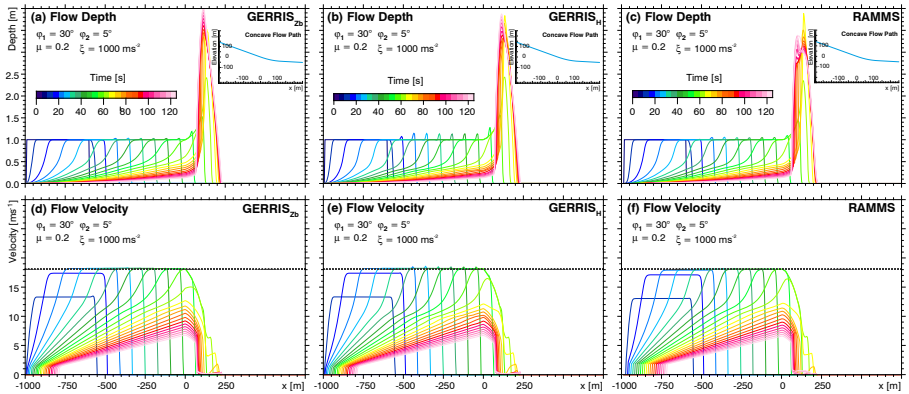

Figure 5. Time series of longitudinal profiles plotted every 5 s for flow depth and flow velocity of the scenario shown in Fig. 4. Profiles are based on numerical solutions of **(a, d)** GERRIS$_{Zb}$ **(b, e)** GERRIS$_{H}$, and **(c, f)** RAMMS. The insets show the topographic profile.

NHESSD
2, 6775–6809, 2014

Modeling rapid mass movements using the shallow water equations

S. Hergarten and J. Robl

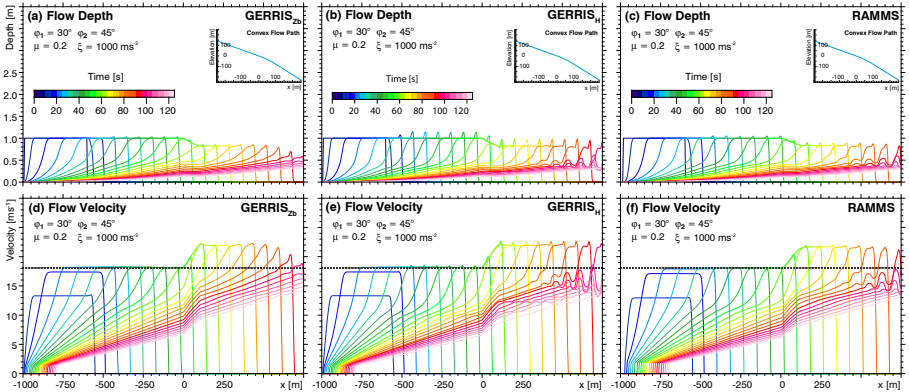

Figure 6. Time series of longitudinal profiles plotted every 5 s for flow depth and flow velocity of a granular fluid on a convex slope with $\varphi_1 = 30^\circ$, $\varphi_2 = 45^\circ$ and a smooth transition between the two segments. Profiles are obtained from numerical solutions of **(a, d)** GERRIS$_{Zb}$ **(b, e)** GERRIS$_{H}$, and **(c, f)** RAMMS. The insets show the topographic profile.

NHESSD
2, 6775–6809, 2014

Modeling rapid mass movements using the shallow water equations

S. Hergarten and J. Robl

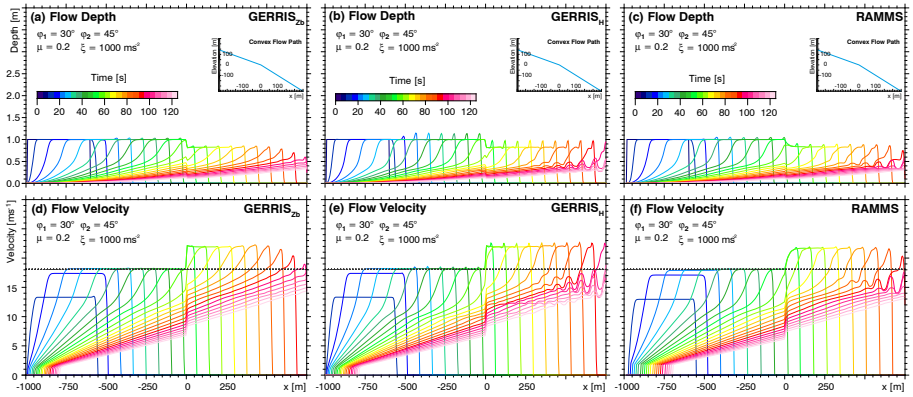

Figure 7. Time series of longitudinal profiles plotted for the scenario considered in Figs. 6 and 7, but with a sharp transition between the planar slope segments.

NHESSD
2, 6775–6809, 2014

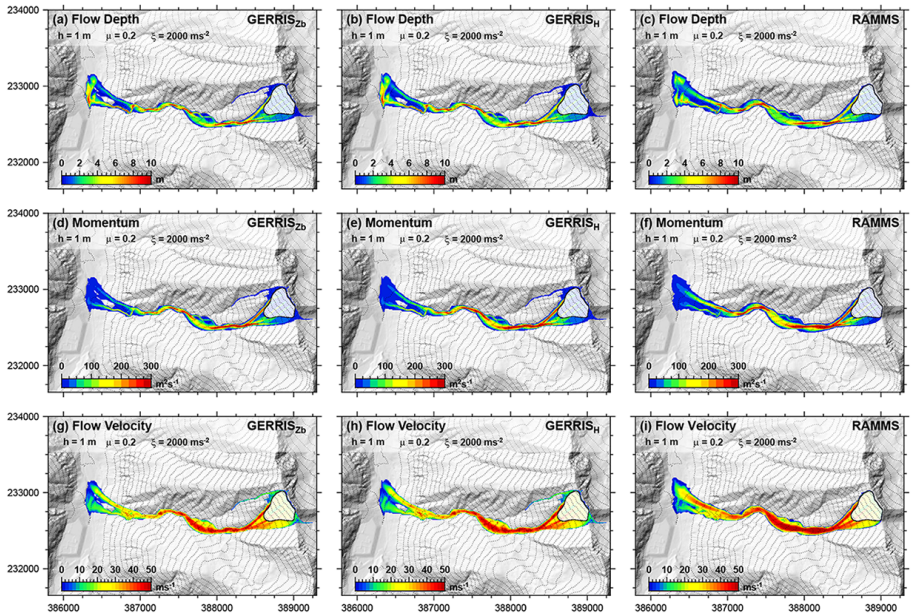

Figure 8. Maximum values of the characteristic properties of a hypothetical avalanche flowing along a curved and twisted thalweg on a real topography (Felbertal, Austria), based on the numerical solutions of GERRIS$_{Zb}$, GERRIS$_{H}$, and RAMMS for the same model set-up. Fluid rheology ($\mu = 0.2$, $\xi = 2000\,\mathrm{m\,s^{-2}}$) and spatial resolution for the three different numerical models are the same. **(a–c)** maximum flow depth, **(d–f)** maximum momentum, **(g–i)** maximum flow velocity.

NHESSD
2, 6775–6809, 2014